CCFE
CULHAM CENTRE FOR FUSION ENERGY

UK Atomic Energy Authority

UKAEA-CCFE-PR(24)206

O. Myatra, B. Lipschultz, D. Moulton, K. Verhaegh, B. Dudson, S. Orchard, A. Fil, C. Cowley

The role of divertor magnetic topology in detachment control in the MAST-U Super-X geometry

The role of divertor magnetic topology in detachment control in the MAST-U Super-X geometry

O. Myatra, B. Lipschultz, D. Moulton, K. Verhaegh, B. Dudson, S. Orchard, A. Fil, C. Cowley

This is a preprint of a paper submitted for publication in
Plasma Physics and Controlled Fusion

The role of divertor magnetic topology in detachment control in Super-X configurations

O. Myatra[a,b], B. Lipschultz[b], D. Moulton[a], K. Verhaegh[a], B. Dudson[b], S. Orchard[a,b], A. Fil[a], C. Cowley[a,b]

[a] *Culham Centre for Fusion Energy, Culham Science Centre, Abingdon, OX14 3DB, United Kingdom*
[b] *York Plasma Institute, University of York, Heslington, York, YO10 5DQ, United Kingdom*

Abstract

Control of the detachment front between the target and the X-point is necessary for minimizing the effect of detachment on the core plasma (core radiation and loss of confinement) and maximizing the divertor functions (reduction of target heat load and sputtering, He pumping). However, such control has been difficult in experiments. The SOLPS-ITER code has been utilised to study the issue for MAST-U Super-X plasmas where detachment is achieved through two separate scans of 'control' parameters - outboard upstream density (n_u) and the divertor impurity concentration (f_I). We find for either n_u or f_I scans that initially, as in current tokamaks, the detachment front moves quickly away from the target after detachment onset. However, in the Super-X geometry studied here, the sensitivity of detachment front location (in a normalised parallel space), z_f, to the controls drops significantly in a region of high parallel gradients in the total magnetic field in the divertor. A simplified analytical model of the sensitivity of the detachment front movement to controls including n_u and f_I has been generalised to obtain z_f for an arbitrary divertor total magnetic field profile and applied to the case studied here. We find that the model approximates the SOLPS results for both scans - a significant drop in the sensitivity of the front location to is predicted in a region of high parallel gradients in the total magnetic field. However, it is found that the significant drop in sensitivity in parallel space translates to a relatively mild reduction in sensitivity in poloidal space. Such slowing down and/or stopping of the detachment movement, if further substantiated, could provide a route to much improved control and the potential to passively stabilizing the detachment location in the strong region for a wide range of core plasma transients.

Keywords: Tokamak divertor; Detachment control; MAST-U; Super-X; SOLPS-ITER

1. Introduction

An important challenge standing in the way of commercial fusion power is mitigating high heat and particle fluxes delivered to plasma facing components (called 'divertor targets') in tokamaks [1, 2]. A phenomenon called 'divertor detachment' has been shown to give large reductions of plasma pressure at the target and concomitant drops in parallel heat and particle fluxes reaching the target [3] - it is likely that commercial tokamaks will need to operate in the detached regime [4].

Detachment initiation requires low plasma temperature at the target (typically $\leq$ 5eV) - this is normally achieved by increasing the outboard mid-plane density or introducing impurities which radiatively dissipate heat in the divertor [5, 6, 7]. Following detachment onset, a roughly uniform low pressure and temperature region expands away from the target towards the X-point. The upstream end of that cold region is called the detachment front which is contiguous to the low temperature edge of the 'thermal front' - a region of steep temperature gradients driven by power losses from the flux tube in which the temperature transitions between the hotter upstream region and either the target (when attached) or the detachment front after detachment. The detached region is dominated by recombination and other neutral processes [8]. The high radiation of the thermal front is often observed to move all the way to the X-point [9]. The presence of a low temperature region at the X-point can lead to varying degrees of core energy confinement degradation; either directly by introducing a cold region next to, or inside the separatrix; or indirectly, through easier penetration of neutrals and impurities across the separatrix [10, 11, 12]. Although X-point radiation without much loss of energy confinement has been achieved in ASDEX Upgrade, this may not be applicable for future machines operating closer to the L-H threshold. The compression/enrichment of impurities and neutrals in the divertor has

also been found to degrade during detachment, which can result in core contamination and also raises concerns for pumping helium in a reactor when the divertor is fully-detached [13, 14]. It is therefore important to identify the optimal detachment front location and to find ways of holding it at this position - feedback control of the detachment front location is a requirement to maintain any such divertor solution.

There have been several successful detachment feedback control experiments using impurity seeding gases for control of outer divertor detachment in H-mode plasmas [15, 16]. However, the detachment front was only held either at the X-point or the target (on the verge of detachment) in these experiments. The ultimate goal is to determine if there is a core and divertor scenario that is compatible with a cost-effective, energy-producing, controllable reactor, and that allows control of detachment. This requires the ability to hold the detachment front anywhere between the X-point and the target - the detachment front location depends on the values of 'control' parameters like the outboard midplane density, n_u, the scrape-off layer impurity density fraction (concentration), $f_I = n_z/n_e$, and power crossing the separatrix into the scrape-off layer, P_{SOL}. Holding the front at any location is thought to be difficult in current devices due to an extremely small 'detachment window'. The detachment window for a control parameter $C = n_u,\ f_I$ *or* P_{SOL} is defined as the range $C_\times - C_t$ where $C_\times$ and C_t are values of C when the front is at the X-point and target respectively. So a bigger detachment window corresponds to better control. An understanding of the dependence of the front location on control parameters is therefore crucial.

This problem has recently been addressed using an analytical model called, herein, the detachment location sensitivity model (DLS) which provides theoretical predictions of the detachment position dependence on three control parameters and the divertor magnetic topology [17]. The model predicts that increasing connection length and decreasing total magnetic field strength, B, from X-point to target increases the detachment window for all control variables. In particular, the sensitivity of the detachment location (in parallel space) to controls is predicted to be inversely proportional to the parallel gradient along the magnetic field in the divertor (i.e. improved control in regions of strong parallel B-field gradients). This implies that the ability to control detachment will likely depend on divertor magnetic topology (and hence geometry). Advanced divertor configurations have been proposed which may enhance detachment control and power/particle exhaust through increased poloidal and total magnetic flux expansion and neutral baffling. The upgraded Mega Amp Spherical Tokamak (MAST-U) has been upgraded to test one such configuration for the outer divertor known as the Super-X [18, 19, 20]. The MAST-U divertor design allows for greater control of divertor magnetic topology and improved neutral compression, providing a test bed to study detachment physics.

In this work, the SOLPS-ITER code package [21] has been used to perform two parameter scans to transition from attached (high-recycling) to strongly detached conditions in MAST-U in the Super-X geometry [22], with a focus on the role of parallel B field gradients in detachment control. The first is performed at fixed input power, with the main ion fuelling rate varied (with no extrinsic impurities) to obtain a scan in the upstream density, n_u. The second detachment scan varies the divertor impurity fraction, f_I, by varying the seeding rate of an extrinsic impurity (nitrogen) at a fixed fuelling rate. Note that for both the seeding and fuelling scans there is a background level of carbon due to plasma sputtering the first wall surfaces which are made of carbon.

For each set of the steady state detached solutions obtained, movement of various detachment location markers is tracked as a function of main ion and impurity injections rates. In both cases we observe a drop in the sensitivity of the detachment location to controls (increasing n_u or f_I) in a region of high parallel gradients in the total magnetic field, B. In the DLS model, only a linear variation in the divertor B field is considered, unlike what occurs in MAST-U. To address this limitation in the current application of the model, the DLS model is generalised to obtain predictions for arbitrary B-field variation in the divertor, and applied to the MAST-U Super-X geometry. We find that the DLS model, in agreement with SOLPS results, predicts a significant reduction in sensitivity of the detachment location in parallel space to controls in a region of high parallel gradients in B. Said another way, the movement along a flux tube for a fixed increment in N_2-seeding or D_2-fuelling decreases as the region of high parallel gradients in B is reached. Such slowing down of the detachment movement, if further substantiated, could provide a route to improved control of the detachment location. Ideally, further studies also lead to a divertor design where the detachment location is passively-stable to a wide range of core plasma transients. The research presented herein may help guide improvements in the DLS model which can then serve as a tool for the future divertor design and optimisation.

The simulation setup and movement of some of the detachment front markers as a function of impurity seeding rate and main ion fuelling rate (the only input parameters varied in these scans) are both described in more detail in the following section. The DLS model is briefly described in section 3 and predictions are compared with the movement

of detachment front markers in SOLPS. Some of the limits/caveats associated with comparing the predictions of this simplified model with SOLPS simulations are described in section 4. Conclusions and future directions are summarised in section 5.

2. SOLPS-ITER simulations of the MAST-U Super-X divertor

2.1. Simulation setup

As mentioned above, SOLPS-ITER is utilized in the studies described in this paper. The plasma simulation domain is shown in figure 1 and it corresponds to a Super-X divertor equilibrium similar to the ones used for previous MAST-U studies using SOLPS [22, 23]. In the analysis presented in further sections, we focus on the flux tubes that deliver the peak heat and particle fluxes to the target (in the attached phase), SOL rings 2 and 5 respectively, which are highlighted.

The plasma boundary conditions chosen in these simulations are identical to the ones presented in [22]. The total power entering the domain through the core boundary is 2.5MW in each scan. In all cases, the cross-field heat diffusivity, $\chi_\perp = 10$ m^{2}s^{-2} and particle diffusivity, $D_\perp = 0.2$ m^{2}s^{-2} are used everywhere except in a small region inside the core where, to emulate H-mode temperature and density pedestals, we have used $\chi_\perp = 2$ m^{2}s^{-2} and $D_\perp = 0.02$ m^{2}s^{-2}. These diffusivities give radial SOL widths of $\lambda_q = 6$mm, $\lambda_n = 17$mm and $\lambda_{T_e} = 24$mm, similar to values found in MAST H-mode experiments [24, 25, 26].

The default set of neutral reactions is used [27], with the addition of nitrogen ionisation (AMJUEL H.4,10 2.7A0) in the seeding scan. The code was run with neutral-neutral collisions, impurity neutralisation and drifts turned off (assuming zero current). Intrinsic carbon is included as a sputtered impurity in both scans, with 3% chemical sputtering yield. In the fuelling scan, D_2 molecules are injected from the inboard midplane. The fuelling rate is varied from $1 \times 10^{21} - 1.1 \times 10^{22}$ D_2 s^{-1} and for the impurity seeding scan, a case just before roll-over of the total target current is chosen from the fuelling scan (fuelling rate = 2×10^{21}). Nitrogen atoms are injected into the divertor, close the entrance as shown in figure 1 (up-down symmetric). Nitrogen seeding rate is varied from $5 \times 10^{19} - 1.1 \times 10^{21}$ N s^{-1}. In each scan, steady state solutions are obtained for each fuelling or seeding rate.

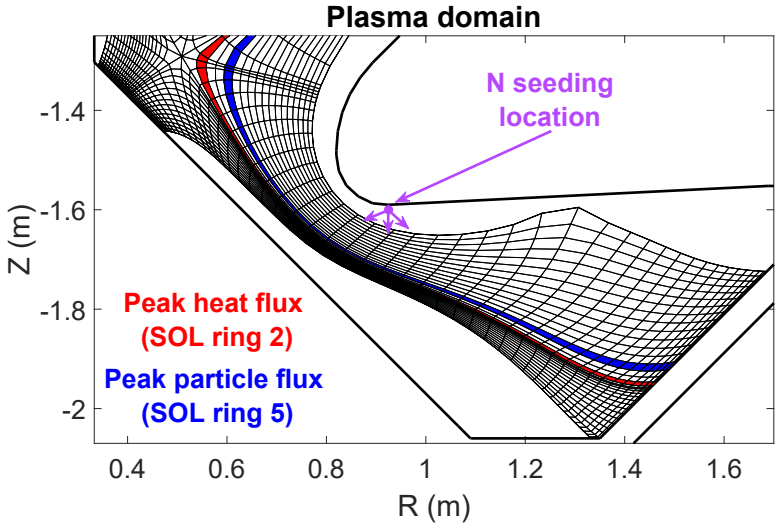

Figure 1: Divertor plasma simulation grid and nitrogen seeding location. Flux tubes are highlighted which correspond to the maximum heat (red) and particle flux (blue) to the target when fuelling rate = $2 \times 10^{21} D_2$ s^{-1} are chosen for analysis.

2.2. Movement of detachment location in the poloidal plane

Detachment is typically accompanied by a variety of changes in the divertor, e.g. pressure loss through interactions with neutrals due to the low ($T_e \leq 5$eV) temperatures and the movement of impurity and hydrogenic radiation peaks. In experiments, a target electron temperature of 5eV is normally utilized as a threshold for detachment, after which

various divertor characteristics change [3, 28]. For example, various radiation profile peaks (hydrogenic, impurity or total) move towards the X-point. Researchers have tracked the location of the point where the C-III radiation drops to $1/e$ or 50% of the maximum towards the target [9, 29, 30], using that location as a rough proxy of the detachment region's front edge (detachment location). These quantities can also be tracked in SOLPS-ITER simulations. Unlike experiments, the 5eV point can also be tracked using the SOLPS output which we track along with the location of the peak power losses due to hydrogenic radiation (excitation plus ionization, P_H) and due to total impurity radiation (due to carbon in the fuelling scan, P_C; and both nitrogen and carbon in the seeding scan, P_{C+N}). In addition, we track the locations at which these power losses drop to 50% of their maximum value on the target side of the peak. It should be noted here that in reality the front is a rather nebulus thing and therefore we can't strictly define it. This is the reason why we choose to follow several definitions to see if they behave similarly.

We find that in general, movement of the quantities tracked slows down as a function of D_2 fuelling or N seeding rate, as their location approaches a region of high parallel gradient in B which is also near the baffle or divertor entrance. The evolution of the T_e = 5eV contours in the poloidal plane is shown in figures 2(a) and (b) for each detachment scan. It can be seen that as the 5eV boundary approaches the region of high parallel gradient B (shaded in grey), the sensitivity of its location to changes in the injection rate drops in both scans. A similar trend is observed in the movement of hydrogenic and impurity power loss peaks, but not shown. Figures 2(c)-(e) show the evolution of poloidal profiles of T_e, P_H and P_{C+N} from SOL ring 5 of the seeding scan. The movement of the P_H and P_{C+N} peaks, as well as the points at which P_H and P_{C+N} fall to 50% of maximum on the target side, are shown to also slow down for increasing seeding rate.

It is interesting to note the relative positions of the various possible detachment markers along the P_H and P_{C+N} profiles in figures 3(c) and (d). The T_e = 5eV point typically lies close to 50% of the peak of the P_{C+N} and P_H profiles (side towards the target).

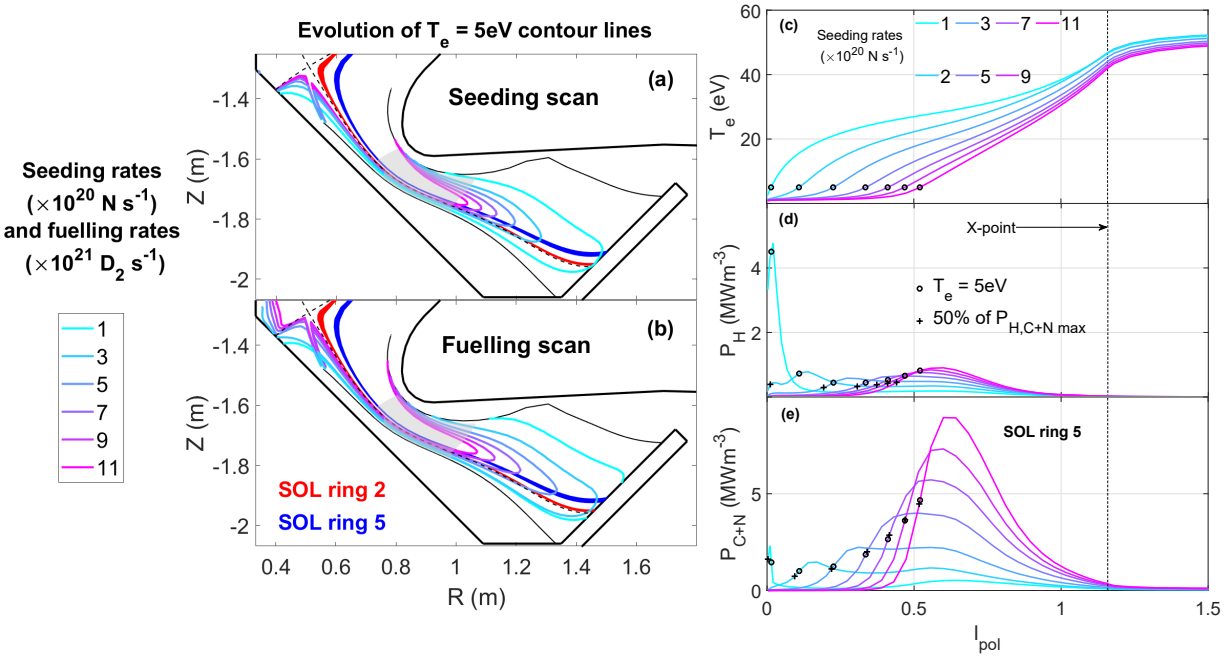

Figure 2: ((a) and (b)) Evolution of T_e = 5eV contour lines for seeding and fuelling scans. The region in which the parallel gradient in B is greater than 50% of the maximum in the divertor is shaded in grey; (c, d and e): Profiles of T_e, P_H and P_{C+N} are shown as a function of l_{pol} for the seeding rate scan to detachment. In addition markers are added to denote the T_e = 5eV points (circles), as well as the location where P_H and P_{C+N} drop to 50% of maximum (crosses). Also highlighted are the model grid flux surfaces corresponding to the peak heat flux (red) and peak particle flux (blue).

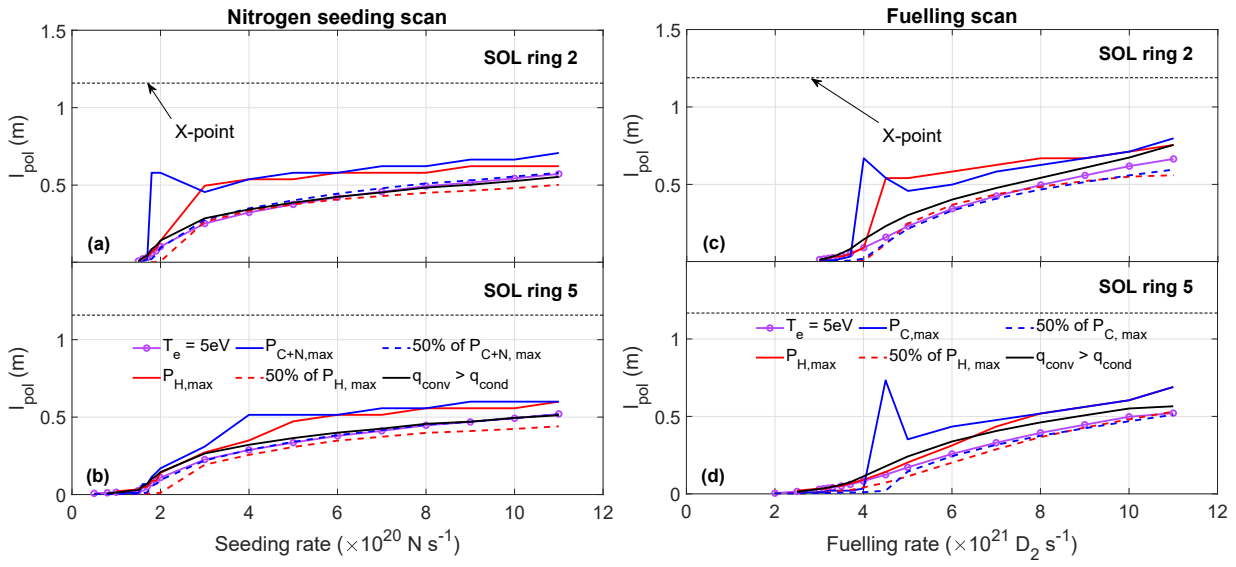

Figure 3: The movement of the detachment front in poloidal plane, l_{pol}, for nitrogen seeding scan (a and b) as well as the D2 fuelling scan of the upstream density (c and d): 6 different 'markers' corresponding to the detachment front location are shown.

The general reduction in sensitivity of the various potential detachment location markers to the injection rates is shown more clearly in figure 3 which displays the l_{pol} location of the various markers introduced above as a function of seeding and fuelling rate for the two SOL rings. In general, the 5eV marker leaves the target shortly after the radiation peaks leave the surface ($l_{pol} > 0$). The 5eV markers are only a short distance downstream in l_{pol} from the radiation peaks for most injection rates. In both scans, locations of the 50% of $P_{H,max}$ and $P_{C,max}/P_{C+N,max}$ points leave the target at shortly after the 5eV point in the fuelling scan, but quickly 'catch up' and either coincide with the 5eV point or are very close it through most of the scan.

One of the changes in the divertor that is accompanied by the low temperatures is the significant reduction in the heat transported by conduction. We find that around detachment temperatures, heat conduction drops to a point where convection becomes the dominant heat transport mechanism. In addition to the detachment markers discussed above, we also track the point where heat convection dominates over heat conduction, shown in black in figure 3. It is interesting to see that this point also typically lies close to the 5eV and 50% points through out both scans. As mentioned earlier, the front is actually rather nebulous and hard to strictly define. Heat convection is neglected in the DLS model, so for computational studies which have access to significantly more information on the plasma parameters compared to experiment, this point where heat convection dominates over conduction could serve as a physics based hard boundary marking the start of the detached region.

The reader will note that the markers for the radiation peaks can abruptly move to larger l_{pol} for small changes in seeding or fuelling rates. This can be traced back to the profiles of radiation in figures 3(d) and (e). At low fuelling/seeding rates there can be two peaks in the profiles of P_{C+N} and P_H, one near the target, and the other upstream at $l_{pol} \approx 0.5 - 0.7$m. As the seeding is increased, the peak near the target drops and the peak upstream grows and thus the location of the higher peak changes abruptly from near the target to further towards the x-point. The peak near the target drops because the temperature there is dropping and both impurity and hydrogenic sources of radiation drop at detachment temperatures ($T_e \leq$ 5eV). Therefore in this work, for simplicity, we consider the flux tube to be 'detached' when the 5eV point leaves the target.

In summary, a reduction in the sensitivity of the plasma profiles to impurity seeding and main ion fuelling rates is observed as increasing power loss occurs in a region of high parallel greadients in the magnetic field. In the next section, we study the movement of these points as a function of 'physics' control parameters described in the DLS model - we will first briefly describe the key assumptions and model equations, and then compare predictions of the DLS model for MAST-U to the simulation results.

3. Comparison of DLS model and SOLPS-ITER predictions of detachment location

3.1. The modifications of the DLS model to apply to SOLPS data

Our modification of the DLS model for this study is mandated by the need to apply the model to a situation where the variation of $|B|$ along a field line is not linear; certainly true for the Super-x divertor. We follow the development of the DLS model: power balance is used to predict the thermal/detachment front location as a function of n_u, f_I and P_{div}. The front moves along a mathematically convenient parallel co-ordinate z defined such that $z = 0$ at the target and $z = L$ at the outboard midplane. The length z is actually the volume of the flux tube between the target and z normalised by a reference area $\propto (1/B_\times$, $B_\times$ is the magnetic field strength at the X-point) and it is related to the actual parallel distance from the target (l) as:

$$dz = \frac{B_\times}{B} dl = \frac{B_\times}{B_{pol}} dl_p \tag{1}$$

In other words, the element dz is essentially the actual elemental parallel distance dl scaled by the total flux expansion at that point in the divertor. As a result, the regions close to the target (where the total flux expansion is high) are elongated in z space. This is illustrated in figures 4(a) and 4(b) which shows a comparison of z and l for SOL ring 2.

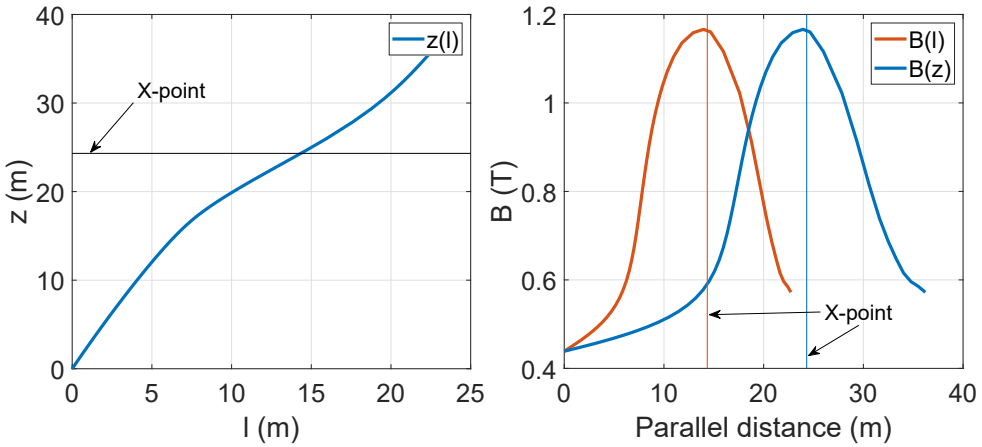

Figure 4: The parallel coordinate z as a function of the actual parallel distance from the target l is shown in figure (a) for SOL ring 2. For this flux tube, B field between target and outboard midplane is shown in figure (b) as a function of both l and z.

The thermal front (within which the radiative power loss occurs) is assumed to be thin/small compared to the distance $z_\times$; in the DLS analytic model that assumption simplifies the calculation of the radiative loss as well as allowing the thermal front (and detachment location) to move a significant amount from $z = 0$ to $z = z_\times$.

The key difference between the DLS model and its application in this study is the treatment of the divertor magnetic field profile; only linear changes in the field between the X-point and target along z are considered in the DLS model in order to simplify the analytic calculations of both the radiation losses and the effect of detachment movement on the upstream temperature.

In the following we have generalized the DLS equations (in particular, equation 27 of [17]) to allow for any divertor magnetic field profile. The detachment front location z_f and the control parameters are related as follows:

$$\frac{n_u \sqrt{f_I}}{P_{div}^{5/7}} = \frac{1}{U} \frac{B(z_f)}{B_\times^{3/7}} \times \left[\int_{z_f}^{z_\times} B^2(z) dz + \int_{z_\times}^{L} \frac{B^2(z)(L-z)}{L - z_\times} dz \right]^{-2/7} \tag{2}$$

where U is assumed to be a constant related to the Lengyel integral [31]:

$$U = 7^{2/7}(2\kappa_0)^{3/14}\sqrt{\int_{T_c}^{T_h} T^{1/2}Q(T)\mathrm{d}T} \tag{3}$$

where $Q(T)$ is the radiative loss parameter [4] and κ_0 is the electron heat conductivity coefficient.

The simplifications made in the analytic DLS model make it difficult to properly compare model predictions to SOLPS results. The power entering the divertor is assumed to be dissipated through radiation due to a single impurity species of constant concentration ($f_I = n_z/n_e$) in the flux tube. In SOLPS simulations, there are multiple radiating species (multiple impurities as well as hydrogen), and their concentrations are not constant along z. There are power loss mechanisms beyond radiation as well. To compare DLS model predictions with the MAST-U simulations presented here, we have utilized an 'effective power loss species concentration', f_{eff}, which is defined (see section 3.2) to account for power losses from multiple impurity species and also the main ion species; f_{eff} is used in place of the impurity concentration f_I. While the gas injection rates are the only parameters varied in the simulations, all three control parameters of the model are affected. Because of this we use a 'lumped' physics control parameter, C_l, which will include simultaneous change in n_u, f_{eff} and P_{div} as the gas injection rate changes:

$$C_l(z_f) \equiv \frac{n_u\sqrt{f_{eff}}}{P_{div}^{5/7}} \tag{4}$$

In our comparison of the DLS model to the SOLPS predictions of detachment location movement, we are interested in comparing the DLS predictions of the *relative* changes in the control parameters. This is consistent with studies of other models using the Lengyel formulation [32] where the prediction of the divertor detachment threshold in f_I was over-predicted by factors ≥ 4. However, the relative tradeoff between control variables in achieving detachment appeared to be accurate.

Further, the examples of applications of the DLS model in the corresponding paper were of the 'window of detachment' in a single control variable; namely the range of a particular control variable that would move the detachment front to the X-point from the target. In the present case the detachment moves from the target to a variable point $z_f < z_\times$ and is affected by multiple control variables. We therefore define a normalised lumped control parameter, $C_{l,norm}$, and take $C_l(z_f = 0)$ to be the value of C_l at the injection rate at which the 5eV point is on the verge of detaching from the target:

$$C_{l,norm}(z_f) \equiv \frac{C_l(z_f > 0)}{C_l(z_f = 0)} = \frac{B_f \times \left[\int_{z_f}^{z_\times} B^2(z)dz + \int_{z_\times}^{L} \frac{B^2(z)(L-z)}{L-z_\times}dz\right]^{-2/7}}{B_t \times \left[\int_{z_t}^{z_\times} B^2(z)dz + \int_{z_\times}^{L} \frac{B^2(z)(L-z)}{L-z_\times}dz\right]^{-2/7}} \tag{5}$$

Changes in C_l and its components as a function of fuelling/seeding rate, relative to their value when the 5eV point detaches, are shown in figure 5. In the seeding scan, changes in C_l are mainly driven by f_{eff} and there is little change in all other quantities. In the fuelling scan, while changes in C_l are driven primarily by n_u, changes in f_{eff} is also significant. The assumed 'constant' U is also shown, and indeed there is little change in this quantity in both scans. Exactly how f_{eff} and U are defined and calculated from the SOLPS output is described in further detail in section 3.2; followed by a comparison of the modified DLS model predictions for MAST-U to the simulation results.

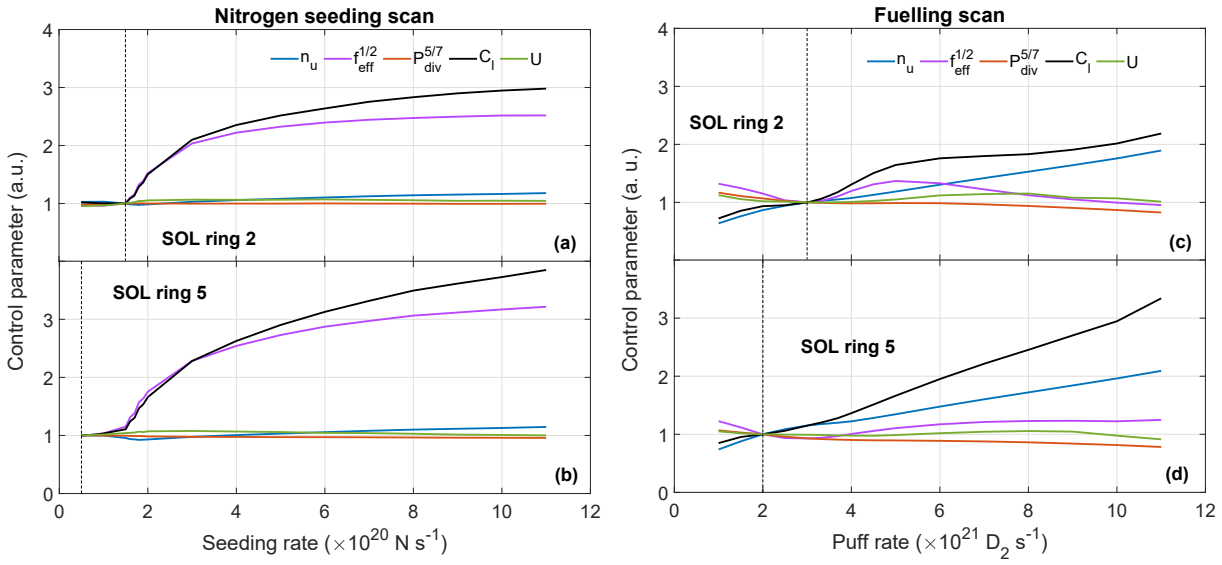

Figure 5: Variation in the lumped control parameter, C_l and its components (all normalised to their value when T_e = 5eV leaves the target) shown as a function of seeding and fuelling rates.

3.2. Extracting SOLPS equivalents of DLS model variables

As mentioned earlier, given that all impurity and hydrogen density fractions vary over the flux tube and the DLS model requires a constant fraction, we developed f_{eff}, a constant along a flux tube. f_{eff} is defined to account for power losses from multiple species (impurity and hydrogenic), each with concentrations varying along the SOL. This is defined using the same framework that the DLS analytical model uses to relate impurity levels and the corresponding power loss. Both the thermal front and DLS models use the function $Q(T)$ that approximates the nitrogen radiation loss parameter to characterize the corresponding radiation power density, P_N, as a function of temperature over the range $1 < T_e < 80$ (and is set to zero outside this range). The constant nitrogen concentration (f_N) that is assumed is defined as:

$$f_N = \frac{\sum_{i=0}^{Z+} n_{N^i}}{n_e} = n_N/n_e \tag{6}$$

The resulting power density is then

$$n_e n_N Q(T) = n_e^2 f_N Q(T) = P_N \ [\mathrm{Wm}^{-3}] \tag{7}$$

To compare SOLPS results to the generalised analytical model, the radiative loss parameter for nitrogen is calculated directly from the SOLPS output:

$$Q_N = \frac{P_N}{n_e n_N} \neq \sum_{i=0}^{Z^+} \frac{P_{N^i}}{n_e n_{N^i}} = \sum_{i=0}^{Z+} Q_{N^i} \tag{8}$$

Note that Q_N is not the sum of the cooling curves associated with each charge state, but more like an effective cooling curve for all the individual charge states of that species.

Now if the impurity fraction f_N were constant in the SOL, then equation 8 can be integrated over the fluxtube to give:

$$f_N = \frac{\int_{fluxtube} P_N dv}{\int_{fluxtube} n_e^2 Q_N dv} \tag{9}$$

To account for the fact that f_N varies along the SOL in SOLPS, an 'effective' constant nitrogen fraction required to dissipate the power that is radiated in that flux tube can be defined as follows:

$$f_{eff,N} = \frac{\int_{fluxtube} P_N dv}{\int_{fluxtube} n_e^2 Q_N dv} = \frac{\int_{fluxtube} P_N dv}{\int_{fluxtube} n_e \frac{P_N}{n_N} dv} \tag{10}$$

Having defined a logic that works for nitrogen, we turn our attention to allowing for additional species, e.g. carbon and/or deuterium. We determine an 'effective' constant radiating species fraction, f_{eff} in a similar fashion to that shown for nitrogen:

$$f_{eff} = \frac{\int_{fluxtube} [P_H + P_C + P_N]\, dv}{\int_{fluxtube} n_e^2 Q_{HCN} dv} \tag{11}$$

where

$$Q_{HCN} = \frac{P_C + P_N + P_H}{n_e(n_C + n_N + n_H)} \tag{12}$$

In fact, Q(T) defined as in equation 12 is used to calculate the constant U in the DLS model (equation 3). Quantities on the RHS of equation 12 are obtained directly from the code and the integral in equation 3 is from the target to outboard midplane. With these definitions, in the case where f_N, f_C and f_H are constant, that we recover $f_{eff} = f_N + f_C + f_H$.

Another DLS model parameter, κ_0, must also be abstracted from the SOLPS output. κ_0 is related to a scaled form of parallel heat flux $q = q_{\|} B_{\times}/B$ (where $q_{\|}$ is the parallel heat flux density) as follows:

$$\kappa_0 = \frac{qB^2}{T^{5/2} B_{\times}^2 \frac{dT}{dz}} \tag{13}$$

Note that in our calculation of κ_0 from SOLPS output for use with the DLS model, equation 13 is applied only to the part of the flux tube where the total parallel conducted heat is ten times larger than the total parallel convected heat. Then, the average of the resulting range of κ_0 values calculated is taken to be the value of κ_0 in equation when calculating U (eq. 3).

Therefore, to account for losses from both the main ion species and multiple impurity species, the comparison is carried out by setting f_I in equation 5 to f_{eff}. Including both C and N as well as the D ionization and excitation costs into an effective radiating species fraction does not generally raise the power loss accounted for substantially but does improve agreement with the DLS model predictions. In future high power devices where the power crossing the SOL strongly increase and the SOL parallel heat flux width remains similar, impurity radiation will likely dissipate an overwhelmingly large fraction of the power entering the divertor.

3.3. Comparison of front movement predictions

The 'model prediction' of $C_{l,norm}$ vs z is obtained by taking the range in SOLPS of $C_{l,norm}$ and evaluating the RHS of equation 5 to derive the predicted value of z. This is displayed by the black curve in figure 6.

Also plotted in figure 6 are the z and $C_{l,norm}$ pairs derived from SOLPS at each modelling injection rate (LHS of equation 5), thus providing the various detachment position markers as a function of $C_{l,norm}$.

Our application of the DLS model ('model prediction') predicts that the detachment location should move quickly to the edge of the high dB/dz region (shaded in grey) and then strongly slow down as a function of increasing $C_{l,norm}$. SOLPS results with the various markers also point to a slowing down in z increase at the same edge of the high dB/dz region but the movement from the target is not as 'fast' as predicted for any marker. The peak in hydrogenic losses (and also impurity losses, not shown) moves quickly to the high dB/dz region and slows considerably in each case; the $P_{H,max}$ marker is most like the DLS model prediction for the detachment location. Differences between flux tubes is substantial - detachment location movement is slower (in z) for ring 5, but there is qualitative agreement overall. Differences between SOLPS-ITER simulations and the analytic model will be further explored in the next section.

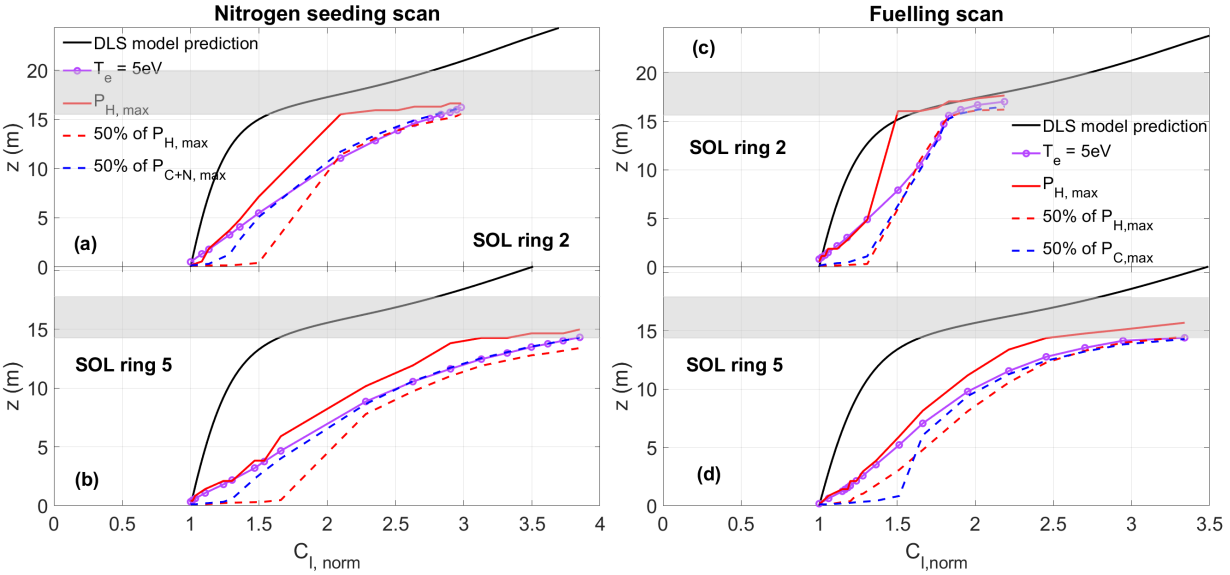

Figure 6: Detachment front location z_f as a function of $C_{l,norm}$ as predicted by the DLS model is shown (black) along with all the position markers that were tracked in l_{pol} in figure 3 for all cases (except $P_{C,max}$ and $P_{C+N,max}$ as they are very similar to $P_{H,max}$ in both scans). The region in which $dB/dz > 50\%$ of max dB/dz in that flux tube is shaded in grey.

4. Discussion

In section 3 we have described the qualitative agreement between or application of the DLS model and SOLPS simulations. In the following we will discuss reasons for lack of quantitative agreement, which includes a number of potential reasons.

4.1. Differences between energy loss mechanisms included in the thermal front model and SOLPS

It is clear from section 3 that the DLS model, for simplicity and ease of obtaining an analytic solution, ignores power loss mechanisms other than radiation from a single impurity that has a fixed concentration along the flux tube. In SOLPS, multiple processes that remove power from a flux tube are present. The total power dissipated between X-point and target, P_{loss}, is given by equation:

$$P_{loss} = P_{C,tot} + P_{N,tot} + P_{H,tot} + P_{rad.\ trans.} + P_{other} \tag{14}$$

The variations of each of the terms in equation 14 are shown as a function of injection rate in figure 7 for both the N2-seeding and D2-fuelling scans. As expected for the fuelling scan, the hydrogenic power losses (deuterium excitation and ionisation, $P_{H,tot}$) are significant and higher than losses to carbon impurity radiation ($P_{C,tot}$) which only accounts for 10-15% of the losses in both flux tubes.

In the seeding scan, while total radiation due to carbon and nitrogen impurities ($P_{C,tot} + P_{N,tot}$) is the dominant power sink for most seeding rates, hydrogenic losses dominate over impurity radiation at low seeding rates. At high seeding rates, impurity radiation losses account for up to 75% of the losses in SOL ring 5 but not significantly more than half of the overall energy losses from that flux tube in the divertor at lower seeding rates.

Radiative and hydrogenic power losses together do not account for much more than half of the flux tube losses for ring 2 in both detachment scans. Power losses due to radial transport ($P_{rad.\ trans.}$) make a significant contribution, particularly for flux surfaces near the separatrix, ring 2. All other power losses (P_{other}), e.g. due to viscous and compressional effects, only make a small contribution to P_{net}.

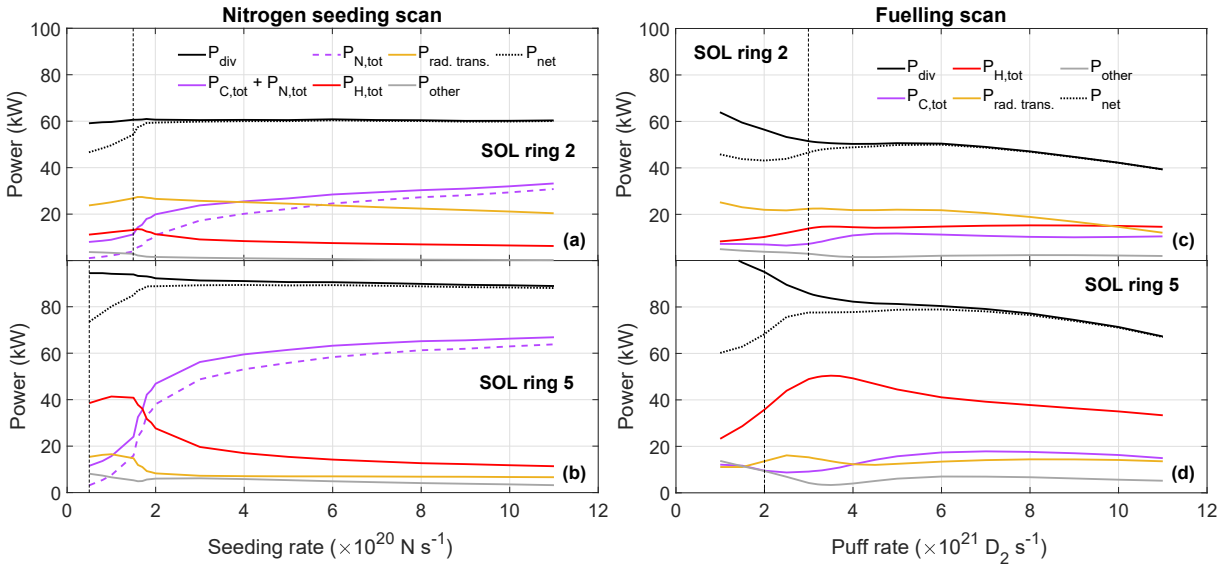

Figure 7: Description of power balance contributors as a function of (a)-(b) nitrogen seeding scan; and (c)-(d) D2 fuelling scan. The total power source entering the flux tubes at the 'X-point' position, P_{div}; total power dissipated between X-point and target, P_{loss}; and the components of P_{loss} (RHS of equation 14). The injection rate at which the 5eV point leaves the target is marked with a vertical dashed line.

4.2. Relationship between dB/dz and movement in l_{pol}

Because of the nature of the DLS model our primary focus up till now is on the movement of the detachment location in z. However, as a practical matter, the operator of a tokamak is interested in the detachment location in l_{pol}, in the poloidal cross-section of the divertor. In figure 8, model predictions shown in figure 6 are mapped from z to l_{pol} using equation 1 and again compared to the movement of the detachment front markers in l_{pol} as a function of $C_{l,norm}$. While the region of high dB/dz occupies only 20%-25% of the space between X-point and target in z, it occupies almost 50% of this space in l_{pol} for the Super-X geometry. As a result, the significant reduction in sensitivity predicted by the model in z space, translates to a milder predicted reduction in sensitivity in l_{pol} space. We note that in the seeding scan, we do observe a reduction in sensitivity of the $P_{iz/rad,max}$ location to changes in $C_{l,norm}$ for both types of scans; that indicates that the thermal front movement, which is ahead of the detachment front, has slowed down as a function of increasing $C_{l,norm}$. However this is not the case for the other markers during the seeding scan. In contrast to the seeding scan, a reduction in sensitivity to controls to increases in $C_{l,norm}$ is observed for all tracked points in the fuelling scan.

The lack of slowing down of the movement of the T_e = 5eV location in the high dB/dz region for the seeding scan is somewhat surprising. Our initial observation of the movement of the T_e = 5eV at or before the high dB/dz region as a function of the seeding rate (figure 2) was that there was a clear slowing down. The difference to the current figure 6 lies in the difference between seeding rate changes and changes in $C_{l,norm}$. f_{eff} changes very little for the same changes in seeding rate at high seeding as compared to that at low seeding.

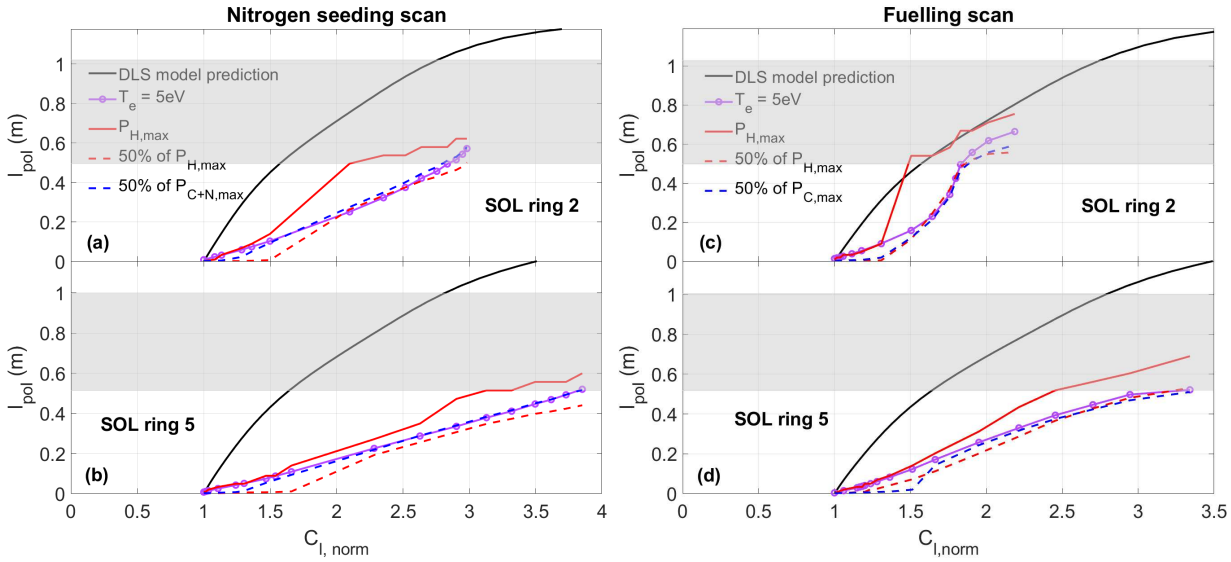

Figure 8: Detachment front location in l_{pol} as a function of $C_{l,norm}$ as predicted by the DLS model and SOLPS. The region where $dB/dz > 50\%$ of the maximum dB/dz is shaded in grey.

4.3. Methods of determining detachment location

Figures 6 and 8 compare various measures of detachment location obtained from the from analysis of the SOLPS-ITER profiles and the DLS model to describe the detachment position between the target and the X-point. SOLPS-ITER is the ideal vehicle for this comparison to ascertain their usefulness, as the quantitative assessment of the various detachment location markers is straightforward compared to experiment.

We find that it is surprisingly difficult to develop a consistent measure of detachment location across a number of choices. Amongst the markers investigated, the T_e = 5eV point seems to have an advantage with SOLPS output due to: a) Physics - the fact that momentum loss dues to charge-exchange collisions becomes dominant over ionization at $T_e \leq 5eV$; and b) It is also simple to determine from the SOLPS solution.

Two of the markers we compared to the DLS model tended to be closer to the X-point than the T_e = 5eV point. Those include the peaks in all the measures of radiation from carbon, nitrogen and nitrogen (figure 6).

For completeness we have also tracked, but not plotted, where the impurity/hydrogenic radiation drops to 50% of maximum $P_{rad,max}$ on the *hot/upstream end of the front* which, for P_{C+N}, corresponds to the leading edge of the thermal front or temperature gradient region. The target, or low-temperature end of the thermal front corresponds to the target itself before detachment and then as the detached region moves off from the target, it is coincident with the forward edge of the detached region. The leading edge of the thermal front is already quite close to the X-point at detachment onset and does not move much throughout both scans due to the rather 'broad' impurity radiation profiles observed during the early stages. Thus, both as observed (figure 6) and expected from the thermal front and DLS models, the thermal front becomes shorter poloidally as the detached region grows.

Further, we find that the distance between the various detachment location markers tracked in the code (figure 6) indicates that the thermal front width/thickness can be comparable to the divertor at the start of detachment, consistent with the thermal front covering a significant fraction of the divertor temperature gradient region. As the front moves off the target, following detachment 'onset', the front starts off thick as it quickly moves away from the target, and gets thinner as it slows down. This is also indicated in the 1D profiles of impurity radiation (figure 2). This kind of variability makes it difficult to properly define the detachment front location. Such a deviation from the model is likely due to the relatively low power entering the scrape-off layer - a similar set of scans at a higher power may reduce this variability. However, given that impurities expected to be used to dissipate power in reactor relevant scenarios (e.g. Ne, Ar, Kr) radiate over a significantly wider temperature range, the front width is likely to increase for these impurities.

4.4. Potential role of baffle

It is possible that the agreement between SOLPS and the location sensitivity model is a coincidence and that there is some other physics slowing the movement of the detachment front towards the X-point or even adding to the dB/dz effect. One possibility is that the baffle plays a role in slowing down the detachment front. In a tightly baffled divertor, the plasma helps to confine the neutrals by plugging the entrance to the divertor. The detachment front then sits slightly inside the entrance to the divertor, in a region of high neutral gas pressure. If the detachment front moved outside the divertor entrance, then the detachment front is in the main chamber, rather than the divertor. The narrow entrance to the divertor is no longer plugged by the plasma, and the neutral gas pressure behind the front drops. To maintain pressure balance, this could cause the front to go back into the divertor, providing a feedback mechanism which would help prevent the detachment front from leaving the closed divertor.

5. Conclusions and future work

Detachment evolution in the MAST-U Super-X geometry has been studied using the SOLPS-ITER, with a focus on the sensitivity of the detachment front location to control parameters. Two sets of steady state solutions were obtained by varying the D_2 and N injections rates at fixed input power (2.5MW), ranging from attached conditions at low injection rates and strongly detached conditions at the highest injection rates (detachment front approximately halfway between X-point and target). Movement of the detachment location is tracked in simulations as a function of physics control parameters and results are compared to predictions of an analytical model.

Both the analytical model (which makes several simplifying assumptions) and SOLPS predict a reduction in the sensitivity of the detachment front location to controls in a region of high dB/dz, which is also close to the baffle. Such a drop in sensitivity, if primarily due to dB/dz, would mean significantly improved detachment control and the potential to passively stabilise the detachment location in the region of high dB/dz for a wide range of core plasma transients. Note that while only dB/dz is important when it comes to controlling the front location, a high $B_\times/B_t$ is still desirable/required to lower the detachment threshold, i.e. to improve detachment access.

The simplifying assumptions also introduce difficulties when it comes to properly comparing predictions with simulation results and likely lead to quantitative disagreement. An ad hoc method is used to account for losses from both main ion species and multiple impurity species of varying SOL density fraction, by adopting the same formalism used by the model to evaluate impurity losses - all impurity and hydrogenic losses are lumped together and associated with an 'effective radiating species fraction'. The detachment front width/thickness is not necessarily small compared to the divertor and can change as the front moves upstream, becomes thinner in the region of high dB/dz. It is likely that these two assumptions are not satisfied due to the relatively low input power and therefore upstream temperature - detachment fronts in future high power devices may satisfy these assumptions, however this also depends on the impurity used to dissipate power. Further studies at higher power and with different impurities like neon or argon are required to assess the validity of these key DLS model assumptions.

It is found that the significant reduction in sensitivity in z space translates to a relatively mild reduction in sensitivity in poloidal space for the divertor geometry considered. It is therefore of interest to repeat this study in a geometry with relatively high $dB/d_{l,pol}$ in divertor.

It is possible that other mechanisms involving the baffle may contribute to the observed reduction in the sensitivity. The potential impact of the baffle on the existing solutions can be studied by modifying the divertor wall geometry or placing virtual surfaces and allowing the solutions to evolve to a new steady state. SOLPS studies in simplified geometries could also help disentangle the potential impact of the baffle from that of dB/dz.

References

[1] A. Loarte, B. Lipschultz, A. S. Kukushkin, G. F. Matthews, P. C. Stangeby, N. Asakura, G. F. Counsell, G. Federici, A. Kallenbach, K. Krieger, A. Mahdavi, V. Philipps, D. Reiter, J. Roth, J. Strachan, D. Whyte, R. Doerner, T. Eich, W. Fundamenski, A. Herrmann, M. Fenstermacher, P. Ghendrih, M. Groth, A. Kirschner, S. Konoshima, B. LaBombard, P. Lang, A. W. Leonard, P. Monier-Garbet, R. Neu, H. Pacher, B. Pegourie, R. A. Pitts, S. Takamura, J. Terry, E. Tsitrone, the ITPA Scrape-off Layer, D. P. T. Group, Chapter 4: Power and particle control, Nuclear Fusion 47 (6) (2007) S203.
URL `http://stacks.iop.org/0029-5515/47/i=6/a=S04`

[2] S. I. Krasheninnikov, A. S. Kukushkin, Physics of ultimate detachment of a tokamak divertor plasma, Journal of Plasma Physics 83 (5) (2017) 155830501. doi:10.1017/S0022377817000654.
URL https://www.cambridge.org/core/product/identifier/S0022377817000654/type/journal_article

[3] B. Lipschultz, B. LaBombard, J. L. Terry, C. Boswell, I. H. Hutchinson, Divertor Physics Research on Alcator C-Mod, Fusion Science and Technology 51 (3) (2007) 369–389. doi:10.13182/FST07-A1428.
URL https://www.tandfonline.com/doi/full/10.13182/FST07-A1428

[4] A. Kallenbach, M. Bernert, R. Dux, L. Casali, T. Eich, L. Giannone, Impurity seeding for tokamak power exhaust : from present devices via ITER to DEMO, Plasma Phys. Control. Fusion 55 (2013) 124041. doi:10.1088/0741-3335/55/12/124041.

[5] B. Lipschultz, J. L. Terry, C. Boswell, J. A. Goetz, A. E. Hubbard, S. I. Krasheninnikov, B. Labombard, D. A. Pappas, C. S. Pitcher, F. Wising, S. Wukitch, The role of particle sinks and sources in Alcator C-Mod detached divertor discharges, Physics of Plasmas 6 (1999) 1907. doi:10.1063/1.873448.
URL https://doi.org/10.1063/1.873448

[6] K. Verhaegh, B. Lipschultz, B. P. Duval, O. Février, A. Fil, C. Theiler, M. Wensing, C. Bowman, D. S. Gahle, J. R. Harrison, B. Labit, C. Marini, R. Maurizio, H. De Oliveira, H. Reimerdes, U. Sheikh, C. K. Tsui, N. Vianello, W. A. Vijvers, An improved understanding of the roles of atomic processes and power balance in divertor target ion current loss during detachment, Nuclear Fusion 59 (12) (2019) 126038. arXiv:1810.04969, doi:10.1088/1741-4326/ab4251.
URL https://iopscience.iop.org/article/10.1088/1741-4326/ab4251

[7] A. Smolders, M. Wensing, S. Carli, H. De Oliveira, W. Dekeyser, B. P. Duval, O. Février, D. Gahle, L. Martinelli, H. Reimerdes, C. Theiler, K. Verhaegh, t. T. Team, Comparison of high density and nitrogen seeded detachment using SOLPS-ITER simulations of the tokamak á configuration variable, Plasma Physics and Controlled Fusion 62 (12) (2020) 125006. doi:10.1088/1361-6587/abbcc5.
URL https://doi.org/10.1088/1361-6587/abbcc5

[8] I. Hutchinson, Thermal front analysis of detached divertors and MARFEs, Nuclear Fusion 34 (1994) 1337–1348. doi:10.1088/0029-5515/34/10/I04.

[9] J. R. Harrison, W. A. Vijvers, C. Theiler, B. P. Duval, S. Elmore, B. Labit, B. Lipschultz, S. H. van Limpt, S. W. Lisgo, C. K. Tsui, H. Reimerdes, U. Sheikh, K. H. Verhaegh, M. Wischmeier, Detachment evolution on the TCV tokamak, Nuclear Materials and Energy 12 (2017) 1071–1076. doi:10.1016/j.nme.2016.10.020.

[10] A. Kallenbach, M. Bernert, M. Beurskens, L. Casali, M. Dunne, T. Eich, L. Giannone, A. Herrmann, M. Maraschek, S. Potzel, F. Reimold, V. Rohde, J. Schweinzer, E. Viezzer, M. Wischmeier, Partial detachment of high power discharges in ASDEX Upgrade, Nuclear Fusion 55 (5) (2015) 053026. doi:10.1088/0029-5515/55/5/053026.
URL https://iopscience.iop.org/article/10.1088/0029-5515/55/5/053026https://iopscience.iop.org/article/10.1088/0029-5515/55/5/053026/meta

[11] G. M. Mccracken, B. Lipschultz, B. Labombard, J. A. Goetz, R. S. Granetz, D. Jablonski, S. Lisgo, H. Ohkawa, P. C. Stangeby, J. L. Terry, Impurity screening in Ohmic and high confinement (H-mode) plasmas in the Alcator C-Mod tokamak, in: Physics of Plasmas, Vol. 4, 1997, pp. 1681–1689. doi:10.1063/1.872365.
URL https://doi.org/10.1063/1.872365

[12] The JET Team, Highly radiating and detached plasmas on carbon and beryllium targets, Plasma Physics and Controlled Fusion 37 (11A) (1995) A227. doi:10.1088/0741-3335/37/11A/015.
URL https://iopscience.iop.org/article/10.1088/0741-3335/37/11A/015https://iopscience.iop.org/article/10.1088/0741-3335/37/11A/015/meta

[13] J. A. Goetz, B. Lipschultz, C. S. Pitcher, J. L. Terry, P. T. Bonoli, J. E. Rice, S. J. Wukitch, Impurity compression and enrichment studies on Alcator C-Mod, Journal of Nuclear Materials 266 (1999) 354–359. doi:10.1016/S0022-3115(98)00582-0.

[14] H.-S. Bosch, W. Ullrich, D. Coster, O. Gruber, G. Haas, J. Neuhauser, R. Schneider, R. Wolf, Helium transport and exhaust with an ITER-like divertor in ASDEX Upgrade, Journal of Nuclear Materials 290-293 (2001) 836–839. doi:10.1016/S0022-3115(00)00539-0.
URL http://linkinghub.elsevier.com/retrieve/pii/S0022311500005390

[15] A. Kallenbach, R. Dux, J. C. Fuchs, R. Fischer, B. Geiger, L. Giannone, A. Herrmann, T. Lunt, V. Mertens, R. McDermott, R. Neu, T. Pütterich, S. Rathgeber, V. Rohde, K. Schmid, J. Schweinzer, W. Treutterer, Divertor power load feedback with nitrogen seeding in ASDEX Upgrade, Plasma Physics and Controlled Fusion 52 (5) (2010) 055002. doi:10.1088/0741-3335/52/5/055002.
URL http://stacks.iop.org/0741-3335/52/i=5/a=055002?key=crossref.cc7cc88ca20e822dd0724980a12286fb

[16] A. Kallenbach, M. Bernert, T. Eich, J. Fuchs, L. Giannone, A. Herrmann, J. Schweinzer, W. Treutterer, Optimized tokamak power exhaust with double radiative feedback in ASDEX Upgrade, Nuclear Fusion 52 (12) (2012) 122003. doi:10.1088/0029-5515/52/12/122003.
URL http://stacks.iop.org/0029-5515/52/i=12/a=122003?key=crossref.b045ee086872468dbaa0a5312962ca08

[17] B. Lipschultz, F. I. Parra, I. H. Hutchinson, Sensitivity of detachment extent to magnetic configuration and external parameters, Nuclear Fusion 56 (5) (2016) 056007. doi:10.1088/0029-5515/56/5/056007.
URL http://stacks.iop.org/0029-5515/56/i=5/a=056007?key=crossref.a45c46af3713ecdd5358a4851aa5f61d

[18] D. Stork, H. Meyer, R. Akers, R. Buttery, I. Chapman, N. Conway, S. Cowley, G. Cunningham, S. Davis, A. Field, The upgrade to the Mega Amp Spherical Tokamak, in: International Atomic Energy Agency (IAEA) Fusion Energy Conference, 2010.
URL https://inis.iaea.org/search/search.aspx?orig_q=RN:43043465

[19] A. W. Morris, MAST: Results and upgrade activities, in: IEEE Transactions on Plasma Science, Vol. 40, 2012, pp. 682–691. doi:10.1109/TPS.2011.2181540.

[20] E. Havlíčková, J. Harrison, B. Lipschultz, G. Fishpool, A. Kirk, A. Thornton, M. Wischmeier, S. Elmore, S. Allan, SOLPS analysis of the MAST-U divertor with the effect of heating power and pumping on the access to detachment in the Super-x configuration, Plasma Physics and Controlled Fusion 57 (11) (2015) 115001. doi:10.1088/0741-3335/57/11/115001.
URL http://stacks.iop.org/0741-3335/57/i=11/a=115001?key=crossref.1189ca7b2936d4104038cb5efefc0dfb

[21] R. Schneider, X. Bonnin, K. Borrass, D. P. Coster, H. Kastelewicz, D. Reiter, V. A. Rozhansky, B. J. Braams, Plasma Edge Physics with B2-Eirene, Contributions to Plasma Physics 46 (1-2) (2006) 3–191.

URL http://dx.doi.org/10.1002/ctpp.200610001

[22] D. Moulton, B. Lipschultz, J. Harrison, Detachment onset in MAST-U according to SOLPS-ITER, in: 44th EPS Conference on Plasma Physics, EPS 2017, no. June, 2017, pp. 1–45.

[23] E. Havlíčková, W. Fundamenski, M. Wischmeier, G. Fishpool, D. Coster, Numerical studies of effects associated with the Super-X divertor on target parameters in MAST-U, Journal of Nuclear Materials 438 (2013) 545–549. doi:10.1016/j.jnucmat.2013.01.113.

[24] A. Kirk, G. F. Counsell, W. Fundamenski, J. W. Ahn, D. Taylor, M. J. Walsh, Y. Yang, A comparison of mid-plane scrape-off-layer measurements with model predictions in MAST and the calculation of cross-field transport coefficients, Plasma Physics and Controlled Fusion 46 (10) (2004) 1591–1603. doi:10.1088/0741-3335/46/10/005.

[25] J. R. Harrison, G. M. Fishpool, A. Kirk, L-mode and inter-ELM divertor particle and heat flux width scaling on MAST, Journal of Nuclear Materials 438 (SUPPL) (2013). doi:10.1016/j.jnucmat.2013.01.074.
URL http://dx.doi.org/10.1016/j.jnucmat.2013.01.074

[26] A. J. Thornton, A. Kirk, Scaling of the scrape-off layer width during inter-ELM H modes on MAST as measured by infrared thermography, Plasma Physics and Controlled Fusion 56 (5) (2014). doi:10.1088/0741-3335/56/5/055008.

[27] V. Kotov, D. Reiter, R. A. Pitts, S. Jachmich, A. Huber, D. P. Coster, J.-E. Contributors, Numerical modelling of high density JET divertor plasma with the SOLPS4.2 (B2-EIRENE) code, Plasma Physics and Controlled Fusion 50 (10) (2008) 105012.
URL http://stacks.iop.org/0741-3335/50/i=10/a=105012

[28] P. C. Stangeby, Can detached divertor plasmas be explained as self-sustained gas targets?, Nuclear Fusion 33 (11) (1993) 1695–1705. doi:10.1088/0029-5515/33/11/I10.
URL https://iopscience.iop.org/article/10.1088/0029-5515/33/11/I10https://iopscience.iop.org/article/10.1088/0029-5515/33/11/I10/meta

[29] C. Theiler, B. Lipschultz, J. Harrison, B. Labit, H. Reimerdes, C. Tsui, W. Vijvers, J. A. Boedo, B. Duval, S. Elmore, P. Innocente, U. Kruezi, T. Lunt, R. Maurizio, F. Nespoli, U. Sheikh, A. Thornton, S. van Limpt, K. Verhaegh, N. Vianello, Results from recent detachment experiments in alternative divertor configurations on TCV, Nuclear Fusion 57 (7) (2017) 072008. doi:10.1088/1741-4326/aa5fb7.
URL http://stacks.iop.org/0029-5515/57/i=7/a=072008?key=crossref.e0ba8c2b73c98effa804e1a3ad432e8c

[30] T. Ravensbergen, M. Van Berkel, S. A. Silburn, J. R. Harrison, A. Perek, K. Verhaegh, W. A. Vijvers, C. Theiler, A. Kirk, M. R. De Baar, The Eurofusion Mst1 Team, The Tcv Team, Development of a real-time algorithm for detection of the divertor detachment radiation front using multi-spectral imaging, Nuclear Fusion 60 (6) (2020). doi:10.1088/1741-4326/ab8183.
URL https://doi.org/10.1088/1741-4326/ab8183

[31] M. Reinke, Heat flux mitigation by impurity seeding in high-field tokamaks, Nuclear Fusion 57 (3) (2017) 034004. doi:10.1088/1741-4326/aa5145.
URL https://mail-attachment.googleusercontent.com/attachment/u/1/?ui=2&ik=21a249e14b&view=att&th=15bf7b74e219c8bf&attid=0.1&disp=inline&safe=1&zw&saddbat=ANGjdJ-sAAkkBC1zEuIUJwdVk6nAioIMuijg5RUo9kzoow1-XJ3J8dq95N_uYVGUffP9ULpViOXaXfq0JFJZqLqUZQWKSLjESaejkWlU0

[32] A. E. Jaervinen, S. L. Allen, A. W. Leonard, A. G. McLean, A. L. Moser, T. D. Rognlien, C. M. Samuell, Role of poloidal E × B drift in divertor heat transport in DIII-D, Contributions to Plasma Physics 60 (5-6) (2020) e201900111. doi:10.1002/ctpp.201900111.
URL http://doi.wiley.com/10.1002/ctpp.201900111